

Tunable Nanoparticle Stripe Patterns at Inclined Surfaces[†]

Suman Bhattacharjee,[‡] Sanjoy Khawas,[¶] and Sunita Srivastava^{*,¶}

[‡]*Centre for Research in Nanotechnology & Science (CRNTS), Indian Institute of Technology Bombay, Mumbai-400 076, India*

[¶]*Soft Matter and Nanomaterials Laboratory, Department of Physics, Indian Institute of Technology Bombay, Mumbai-400 076, India*

E-mail: sunita.srivastava@iitb.ac.in

[†]Preprint

Abstract

Periodic assemblies of nanoparticles are central to surface patterning, with applications in biosensing, energy conversion, and nanofabrication. Evaporation of colloidal droplets on substrates provides a simple yet effective route to achieve such assemblies. This work reports the first experimental demonstration of patterns formed through stick-slip dynamics of the three-phase contact line during evaporation of gold nanoparticle suspensions on inclined substrates. Variation in nanoparticle concentration and substrate inclination alter the balance of interfacial and gravitational forces, producing multiple stick-slip events that generate periodic stripes. Stripe density exhibits a sinusoidal dependence on inclination angle, while inter-stripe spacing remains nearly invariant. Independent control over inter-stripe spacing is achieved through adjustment of nanoparticle or surfactant concentration. These results highlight the complex interplay of gravitational and interfacial forces in directing periodic nanoparticle assembly and establish a versatile, programmable framework for surface patterning with tunable nano/microscale dimensions.

1 Introduction

The ability to direct nanoparticles into well-defined patterns through self-assembly plays a vital role in developing next-generation nanotechnologies. Droplet evaporation-based self-assembly offers a simple, low-cost approach for the creation of ordered structures,¹⁻⁶ though challenges in reproducibility and structural control persist. Ordered ring or stripe patterns of colloidal particles^{2,7} are central to applications in biosensing,⁸ energy conversion,⁹ and advanced printing and patterning technologies,^{10,11} and are the focus of this study. The formation of stripe patterns is intricately linked to the dynamics of the three-phase contact line (TPCL) during solvent evaporation. The TPCL undergoes a series of pinning-depinning events, which significantly influence the final deposition pattern, often leading to the formation of multiple rings or stripes besides a primary coffee-ring.

A diverse array of experimental methodologies in sessile droplet evaporation has been utilized to fabricate stripe patterns through the modulation of the stick-slip dynamics of the TPCL.^{12,13} Kim and collaborators used high-speed interferometry to directly observe the emergence of stripe patterns as a result of stick-slip activities under the influence of particle wettability.¹⁴ Srivastava *et al.* successfully generated concentric ring structures on hydrophilic silicon (*Si*) surfaces by varying the concentration levels of DNA-coated gold nanoparticles.² Formation of multi-ring or stripe patterns has been reported using other methods like the capillary bridge technique,¹⁵ convective self-assembly,^{7,16} “Ball-on-film” method.¹⁷

Despite prior reports of stripe-like deposits, they offer limited control over stripe dimensions, and the role of gravity in enabling such control remains unexplored. The gravitational influence on inclined droplets and the TPCL dynamics have been a subject of sustained interest, with early theoretical and experimental studies exploring how gravity deforms droplet shape and alters contact line behavior.^{18–28} Early works from Quéré *et al.* demonstrated that droplets can remain pinned on a tilted surface as long as contact angle hysteresis exists, and showed that in the case of small hysteresis, droplet shapes remain close to spherical caps despite the incline.²⁹ These observations were further supported by studies that established linear correlations between the droplet aspect ratio and the extent of contact angle hysteresis,³⁰ helping to quantify the degree of gravitational flattening in relation to surface wettability. A number of computational models have investigated how gravity influences evaporation behavior and solute redistribution. Du and Deegan simulated TPCL deposit variations under tilt using a two-dimensional strip-like droplet approximation.³¹ A very recent study by D’Ambrosio *et al.*³² provided theoretical predictions for the lifetime of sessile and pendant droplets evaporating in various modes of evaporation, such as constant radius, constant contact angle, stick-slip, and stick-jump.

Although there is ample theoretical literature on the gravitational effect on an inclined pure water droplet,^{33–36} studies on particle-laden droplets under gravity require attention so

as to understand the dried pattern formations. Sessile droplets on inclined substrates exhibit distorted shapes and uneven evaporation rates compared to their horizontal counterparts, often undergoing more frequent transitions between evaporation modes.^{37,38} This results in inhomogeneous deposition features, most notably the formation of asymmetric coffee-ring structures, “coffee-eye” or a non-homogeneous deposition.^{39–43} Varagnolo *et al.* reported stick-slip motion of water droplets on a chemically heterogeneous surface,³⁷ but this study lacks any surface patterning possibly due to absence of solutes. In a recent study, Winahard *et al.* demonstrated uniform deposition rising from a homogeneous inclined substrate, as a nanolitre-sized colloidal drop undergoes stick-slip mode of evaporation.¹¹ Stripe patterns were not observed in this case, as the slip time was much greater compared to the stick phase. Beyond fundamental studies, gravitationally influenced evaporation has also found relevance in applied contexts. Hampton *et al.* demonstrated directed colloidal structure formation on tilted surfaces,⁴⁴ while studies on blood droplet drying showed that evaporation geometry affects deposition features relevant to lipid detection and forensic analysis.⁴⁵ However, controlled patterning using inclined substrates remains largely unreported.

In this study, we introduce a gravity-assisted self-assembly method that produces semi-circular strips of spherical gold nanoparticles (AuNPs) with controllable dimensions on silicon substrates. Precise control over nanoparticle concentration and the droplet’s evaporation dynamics on a hydrophilic *Si* substrate is shown to be critical for inducing the oscillatory motion of the TPCL, which leads to the formation of multiple semi-circular stripe patterns within the primary coffee-ring. The oscillatory motion of the TPCL arises from the interplay between surface tension and gravitational forces. The number of stripes formed per unit length (σ) and inter-stripe spacings (λ) can be systematically tuned by varying the substrate tilt angle (ϕ) and adjusting the concentrations of nanoparticles (C_{np}). This work establishes a clear correlation between gravitational and interfacial forces in controlling the resulting stripe morphology. Although previous studies have shown the effect of gravity on inclined colloidal drops, the controlled manipulation of pattern dimensions and the underlying mechanism

have not been addressed, which is the primary focus of this paper. Furthermore, to the best of our knowledge, the use of gravity and surface tension to create controllable patterns has not yet been reported.

2 Results and Discussion

2.1 Droplet evaporation on an inclined plane

In Figure 1, the schematic depicting the experimental setup for droplet evaporation of the colloidal suspension and the corresponding SEM micrographs are shown. In a typical experiment, a $2 \mu L$ colloidal suspension is evaporated on a substrate inclined at various angles as shown in Figure 1. The details for nanoparticle synthesis protocol⁴⁶ and experimental methodology are mentioned in the [Experimental Methods](#). A sessile droplet of colloidal AuNPs on a flat hydrophilic substrate takes the shape of a spherical cap with equal contact angles on both sides of the pinned TPCL ($\theta = \theta_L = \theta_R$), as shown in Figure 1(a). Here, we define the pinned site contact (left) angle as θ_L and the rear side (receding side) contact angle as θ_R . The macroscopic sessile drop geometry in equilibrium is governed by Young's equation,⁴⁷

$$\gamma_{LV} \cos \theta = \gamma_{SV} - \gamma_{SL} \quad (1)$$

where γ_{AB} denotes the interfacial tensions between the liquid-vapour (LV), solid-vapour (SV), and solid-liquid (SL) interfaces, respectively. When an inclination angle ϕ is introduced relative to the horizontal plane, the droplet tilts and deforms under gravity, leading to a shift in the center of mass (c.m.) towards the direction of the tilt, and results in an asymmetric droplet shape as shown in Figure 1(b). The shape deformation of the droplet can be correlated with $\Delta\theta = \theta_L - \theta_R$. In case of $\phi = 0^\circ$, $\Delta\theta \approx 0^\circ$, whereas as shown in Figure 1(b), for $\phi = 60^\circ$, the estimate of $\Delta\theta$ in experiments was found to be 6° . A standard coffee ring pattern for a droplet on a substrate with $\phi = 0^\circ$ is depicted in the SEM

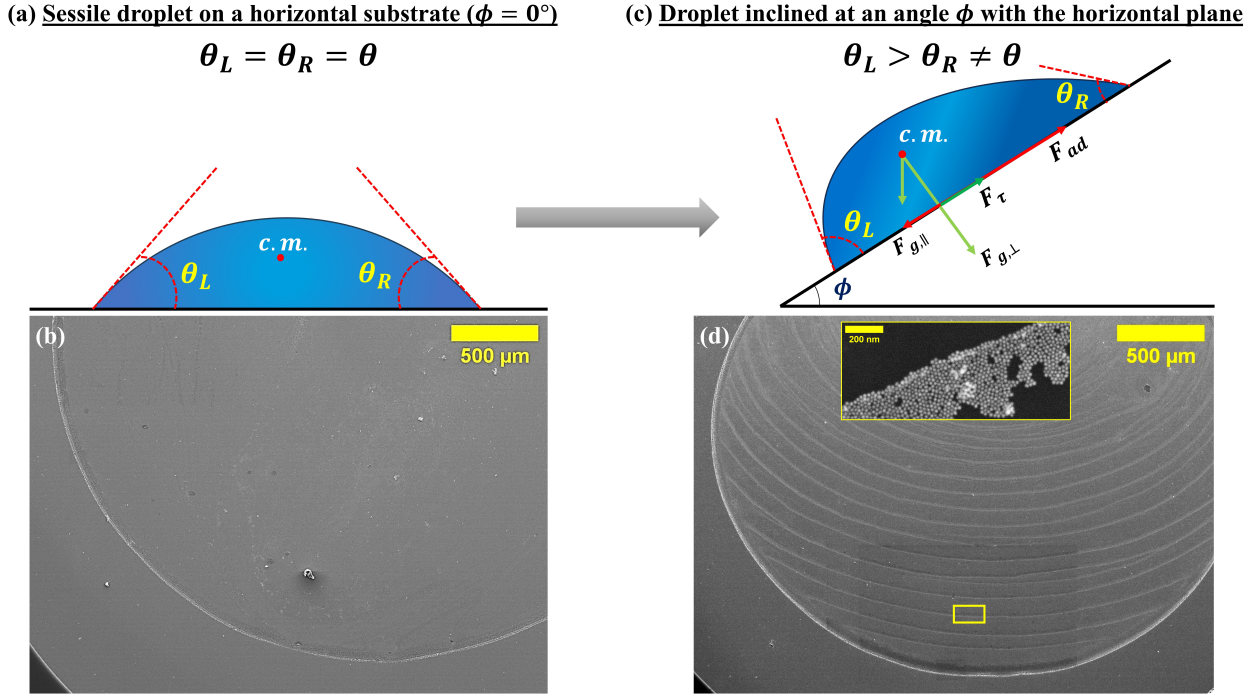


Figure 1: Transition from (a) sessile to (c) inclined droplet configuration resulting in a shift in the center of mass (c.m.). Forces acting on the TPCL, along with the particle flow velocities, are shown. Dried deposit resulting in a coffee-ring (b) for a sessile drop, and ordered stripe patterns after evaporation (d). A typical representation of AuNP deposition on a single stripe (rectangular box) is shown via a high-magnification SEM image in the inset of (d).

micrograph of the dried deposit shown in Figure 1(b). In contrast, the dried pattern for a droplet on a tilted substrate, illustrated in Figure 1(d), displays periodic curved stripes. Hence, here we demonstrate an easy pathway for the creation of tunable microscale patterns with colloidal nanoparticles. Even though particle deposition on inclined substrates has been studied earlier,^{11,40} the formation of such controlled period patterns using nanocolloids has not been reported. Qualitatively, the stripe pattern arises from the stick-slip motion of the TPCL at the elevated edge of the droplet. As the colloidal droplet is tilted, the contact angles gradually decrease during evaporation, triggering geometrical instability. This instability enables the receding section of the TPCL to undergo stick-slip motion,² allowing the formation of AuNP monolayer stripes on the *Si* substrate [Figure 1(d)]. Nevertheless, a detailed quantitative understanding of the driving forces behind this instability is necessary to utilize this approach for programmable and tunable periodic patterning, which constitutes

the focus of the remainder of this paper.

We successfully fabricated microscale AuNP stripes using the inclined droplet evaporation technique; however, questions remain about the controlled tunability of the dimensional features of the resulting patterns. For a sessile drop, gravity exerts a downward force equal to the drop's weight (mg) acting vertically through its center of mass (c.m.). When the substrate is inclined, there is an effective component of gravity proportional to $\sin \phi$ [Figure 1(c)]. Such a force component has been reported to result in sliding/slipping of the droplet based on solution-substrate interaction.^{11,48} Interestingly, in our experiments, the TPCL on one side stayed pinned throughout most of the evaporation process, maintaining long-term droplet stability without sliding or slipping. Although the gravitational drag acts through the shifted c.m. of the bulk droplet, the translated component of this force along the TPCL ($F_{g,\parallel}$) governs the stick-slip motion. The force balance for a static inclined droplet through the shifted c.m. can be expressed as,⁴⁸

$$F_{g,\parallel} - F_\tau - F_{ad} = 0 \quad (2)$$

where $F_{g,\parallel} = mg \sin \phi$ is the gravitational force component along the TPCL, F_τ is the shear force at the solid-liquid interface, and F_{ad} is the adhesion force due to interfacial interactions. While $F_{g,\parallel}$ contributes to TPCL slipping, F_{ad} provides the pinning resistance that regulates stick-slip events. F_τ at the droplet base is negligible ($\sim 10^{-12} \text{ N}$) relative to $F_{g,\parallel}$, F_{ad} and can thus be ignored in our experiments.²⁵ From Eq. 2, we can infer that the interplay of forces like $F_{g,\parallel}$ and F_{ad} shall allow a parametric control on varying the dimensional features of the patterns.

2.2 Effect of gravity-induced asymmetry on the stripe pattern morphology

The gravitational drag force $F_{g,\parallel}$ acting on a tilted drop is directly proportional to the substrate inclination. To explore how changes in $F_{g,\parallel}$ influence the stripe dimensions and achieve

tunability, we performed droplet evaporation experiments at different ϕ values ranging from $0^\circ - 180^\circ$. We observe the formation of stripe patterns for all titled substrates ($\phi = 60^\circ, 90^\circ, 120^\circ$), while coffee-ring and coffee-eye structures formed at $\phi = 0^\circ$ and $\phi = 180^\circ$, respectively [Figure S2(a-e)]. Figure 2(a) shows the stripe patterns corresponding to $\phi = 90^\circ$ where maximum influence of gravity is observed ($F_{g,\parallel} = F_{g,max}$ at $\phi = 90^\circ$). To quantify

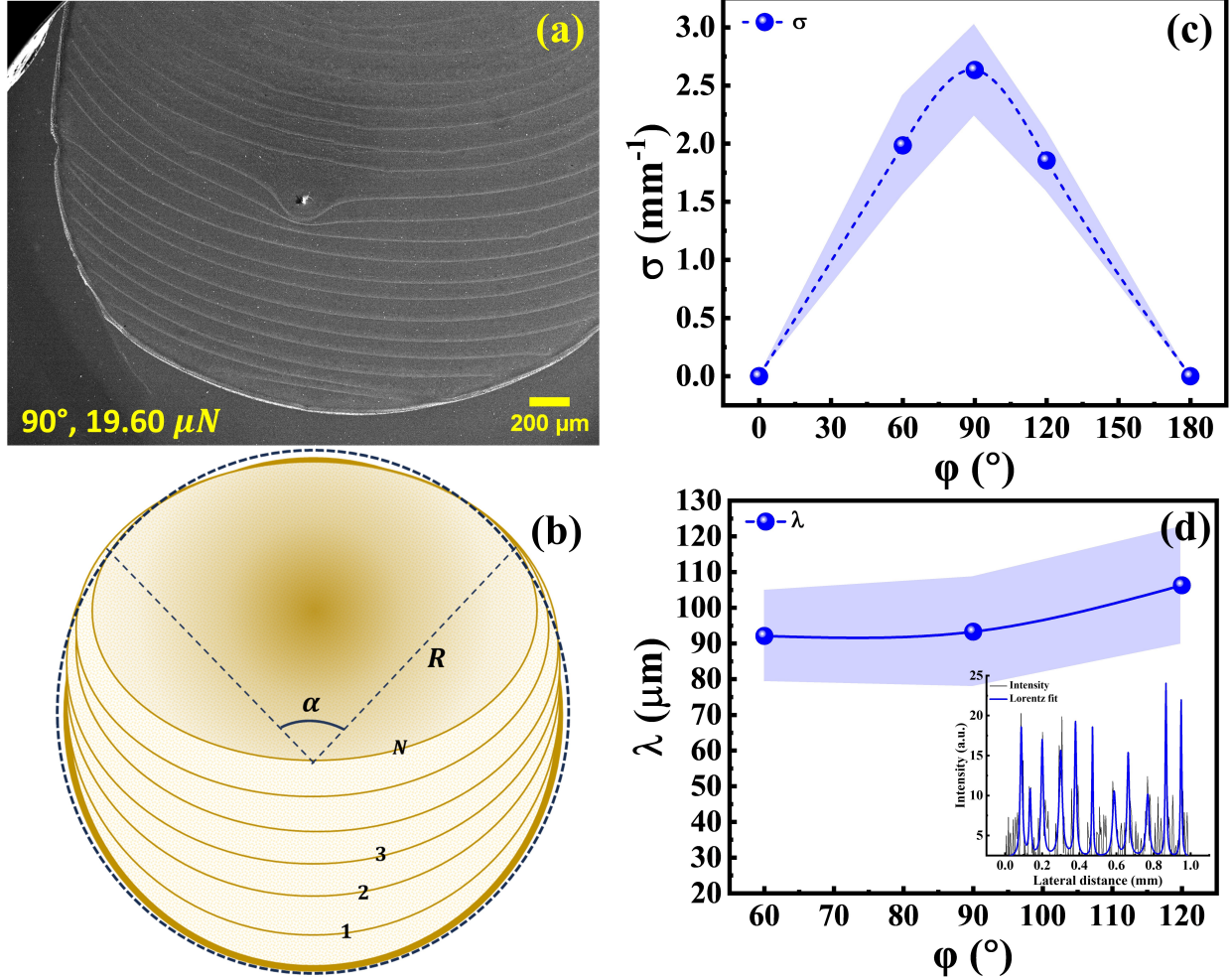


Figure 2: FEG-SEM micrograph of dried AuNP droplet at $\phi = 90^\circ$ (a) is shown here. Schematic (c) shows the fitting technique to obtain σ , λ . Variation of stripe density σ and stripe spacing (λ) with ϕ are plotted in (b,d), respectively. A representative line scan profile from the SEM image is shown in inset (d), where the peak-to-peak distances from the fitted plot are taken as the estimation of λ .

the dimensional features of the stripe patterns, we introduce two parameters: the number of stripes per unit length or the linear stripe density (σ), and the inter-stripe spacing (λ). As

it is observed that the centers of the striped deposits can be different (slips inwards) when we count the stripes away from the TPCL, we developed a fitting process to estimate σ , normalized with the corresponding deposit perimeters, as shown in Figure 2(b). From the circular fitting of the deposit pattern image, the radius R is obtained. Two radii are drawn from the intersection of the last (N^{th}) stripe and the circumference to form the central angle α . For a total of N stripes, the effective length becomes $= \frac{2\pi - \alpha}{2\pi} \times 2\pi R = R(2\pi - \alpha)$, where α is in radians. The linear stripe density σ is therefore given by,

$$\sigma = \frac{N}{R(2\pi - \alpha)} \quad (3)$$

Stripe spacing is calculated as the centre-to-centre separations (λ_i) between the stripes along the radial direction [Figure 2(d) inset], and given by $\lambda = \frac{1}{N} \sum_{i=1}^N \lambda_i$. Figure 2(c) evidently depicts the non-monotonic variation in σ with ϕ . The trend in σ is approximately sinusoidal, at par with the experimental inclinations ($\sigma \sim \sin \phi$). The vertically aligned droplet, which experiences the maximum gravitational drag ($F_{g,max} = 19.6 \mu N$), produces the maximum linear stripe density. The stripe spacing λ exhibits a weak dependence on ϕ , with average estimate of $97.5 \pm 14.6 \mu m$ [Figure 2(d)]. Although the overall trend suggests a slight increase in spacing with increasing ϕ , the large error bars indicate a weak dependence on ϕ , in turn, $F_{g,\parallel}$. The dependence of gravitational force on inclination angle allows for tunability in stripe density, yet the results show that the stripes remain nearly equally spaced. This non-trivial observation prompted us to examine the asymmetric droplet shapes more closely for better insight.

We analyzed the droplet shapes (*in situ*) to understand the effect of gravitational forces on the droplet instability and hence the AuNP stripes. Figure 3(a-e) shows drop shape images at various tilting angles, $\phi \in [0^\circ, 180^\circ]$ for AuNP droplets of concentration $C_{np} = 15 nM$. These droplet images were taken using a camera connected to the tensiometer, immediately after the substrate inclination was introduced. Asymmetric drop shape analysis provides information

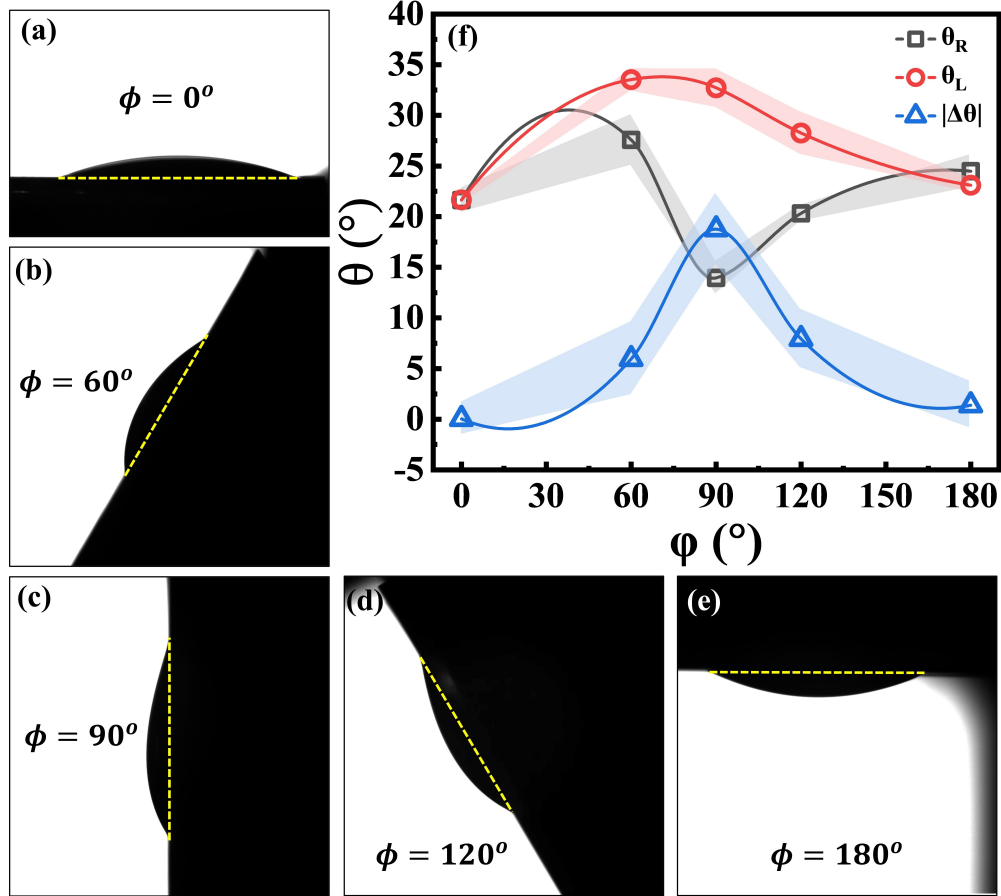


Figure 3: Drop shape images recorded by optical tensiometer with varying gravity effect by changing the inclination angle ϕ (a-e). Dependence of θ_L , θ_R and $\Delta\theta$ on ϕ are shown in (f).

about derived parameters like θ_L and θ_R , as well as intrinsic parameters like droplet radius (R).⁴⁹ As expected, the droplet's TPCL for the sessile ($\phi = 0^\circ$) and pendant drop ($\phi = 180^\circ$) configuration remains pinned at both ends with $\theta_L \approx \theta_R$.^{2,42} The other configurations result in asymmetric droplet shapes as evident from the estimates of θ_L , θ_R , and non-zero $\Delta\theta$ shown in Figure 3(f). While the sessile and pendant drop configurations do not have much hysteresis ($\Delta\theta \approx 0^\circ$), the effect of gravity in the other configurations is prominent. As ϕ increases from 0° to 90° , θ_R decreases, and more liquid volume is pushed towards the inclined end, creating a bulge-like profile [Figure 3(b-d)]. The sinusoidal trend of the direct gravity effect ($\Delta\theta \sim \sin \phi$) is evident from the similar hysteresis for supplementary angles like $\phi = 0^\circ$, 180° and $\phi = 60^\circ$, 120° [Figure 3(f)]. The largest hysteresis is obtained at $\phi = 90^\circ$, suggesting

the maximum downward drag ($F_{g,max} = 19.6 \mu N$) due to the gravitational component. By correlating σ with $\Delta\theta$ [refer to Figure 2(c), 3(f)], we can quantitatively conclude that the larger the hysteresis due to gravitational drag, the higher will be the stripe density. The effect of gravitational drag is also evident from the estimation of coffee-ring widths (CRW) as presented in Figure S3. The CRW at the left, pinned TPCL (w_L), is always estimated to be equal to or higher than the rear/receding side width (w_R). The similar trends observed in CRW and $\Delta\theta$ with ϕ , confirm that gravity primarily governs the formation of these dried patterns. We demonstrate that while tunability in stripe density is achievable, the gaps between stripes remain largely unaffected by gravity's influence.

2.3 Effect of interfacial tension on stripe pattern formation

As the stick-slip events of TPCL are a mechanical as well as interfacial phenomenon, we aimed at manipulating the TPCL dynamics (pinning-depinning events) to introduce tunability of the deposited stripes in terms of λ . As the pinning force on the TPCL is dependent on the interfacial tension, varying the particle concentration is the simplest way to achieve that tunability. The AuNP concentration C_{np} is directly related to γ_{LV} , which in turn relates to γ_{SL} [Eq. 1]. We studied the concentration effect on the stripe pattern at a fixed inclination ($\phi = 120^\circ$). Figure 4(a-c) shows the dried deposits for $C = 2.5 \text{ nM}$ (no stripe), and $5 \text{ nM}, 15 \text{ nM}$ (with stripes). The corresponding FEG-SEM images for AuNP droplets with $C_{np} \in [1 \text{ nM}, 15 \text{ nM}]$ dried in the same tilted configuration are shown in Figure S2(f-j). Our findings indicate that stripe formation only occurs at concentrations of 5 nM or higher; concentrations below this threshold do not result in stripes. For the estimates of σ and λ we only considered $C_{np} \geq 5 \text{ nM}$. Interestingly, when the stripes were produced through the manipulation of surface tension via the change in nanoparticle concentration, we observed a clear inverse relationship between λ and C_{np} [Figure 4(d)], as opposed to the systems where patterns were produced only via a change in ϕ . As C_{np} increases from 5 nM to 15 nM , the average stripe spacing decreases from $\sim 160 \mu\text{m}$ to $\sim 100 \mu\text{m}$. Concurrently,

σ shows a steady increase with increasing C_{np} [Figure 4(e)], as can be expected from the closely-spaced stripes. We found that increasing the particle concentration allowed clear controllability in σ and λ . The gravitational drag, $F_{g,\parallel}$ on these droplets was kept constant, which reflects in the negligible change in $\Delta\theta$. This is also evident from the slight change in Bond number (0.30 – 0.36), which is the ratio of gravity to surface tension force (refer to SI, Figure S5(a,b)). Furthermore, for concentrations below the threshold of $C_{np} < 5 \text{ nM}$, we hypothesize that after the initial pinning, the colloidal droplet lacks the minimum number of particles necessary to sustain further TPCL pinning; consequently, all particles are deposited within the coffee ring itself. Above the critical concentration of 5 nM, there are sufficient particles in the system to enable multiple stick-slip motions of the TPCL following the initial coffee ring formation. This observation is in line with the work of Srivastava *et al.* where stripe patterns were obtained even at $C_{np} = 2.5 \text{ nM}$ for a sessile drop.² In our experiments, a higher threshold concentration ($C_{np} \geq 5 \text{ nM}$) is required for stripe formation on inclined substrates. This suggests that the gravitational drag along the inclined substrate suppresses repeated stick-slip events at lower nanoparticle concentrations, where TPCL pinning is insufficient.

To understand the origin of the observed surface morphology of the deposit pattern shown in Figure 2(a) and 4(a-c) obtained by varying ϕ and C_{np} respectively, let us have a look at the adhesion force term (F_{ad}), defined in Eq. 2. The solid-liquid interfacial tension (γ_{SL}) is directly related to the adhesion force⁴⁸ as,

$$F_{ad} \propto \gamma_{SL}(\cos\theta_R - \cos\theta_L) \quad (4)$$

γ_{LV} values for the different systems are estimated by the Pendant drop method using an optical tensiometer (refer to SI section 4), and consequently γ_{SL} is calculated from Eq. 1, employing θ_R for the receding end of the droplet. Interfacial tension γ_{LV} decreases with an increase in C_{np} , which in turn increases γ_{SL} [table 1]. Adhesion force (F_{ad}), which is directly

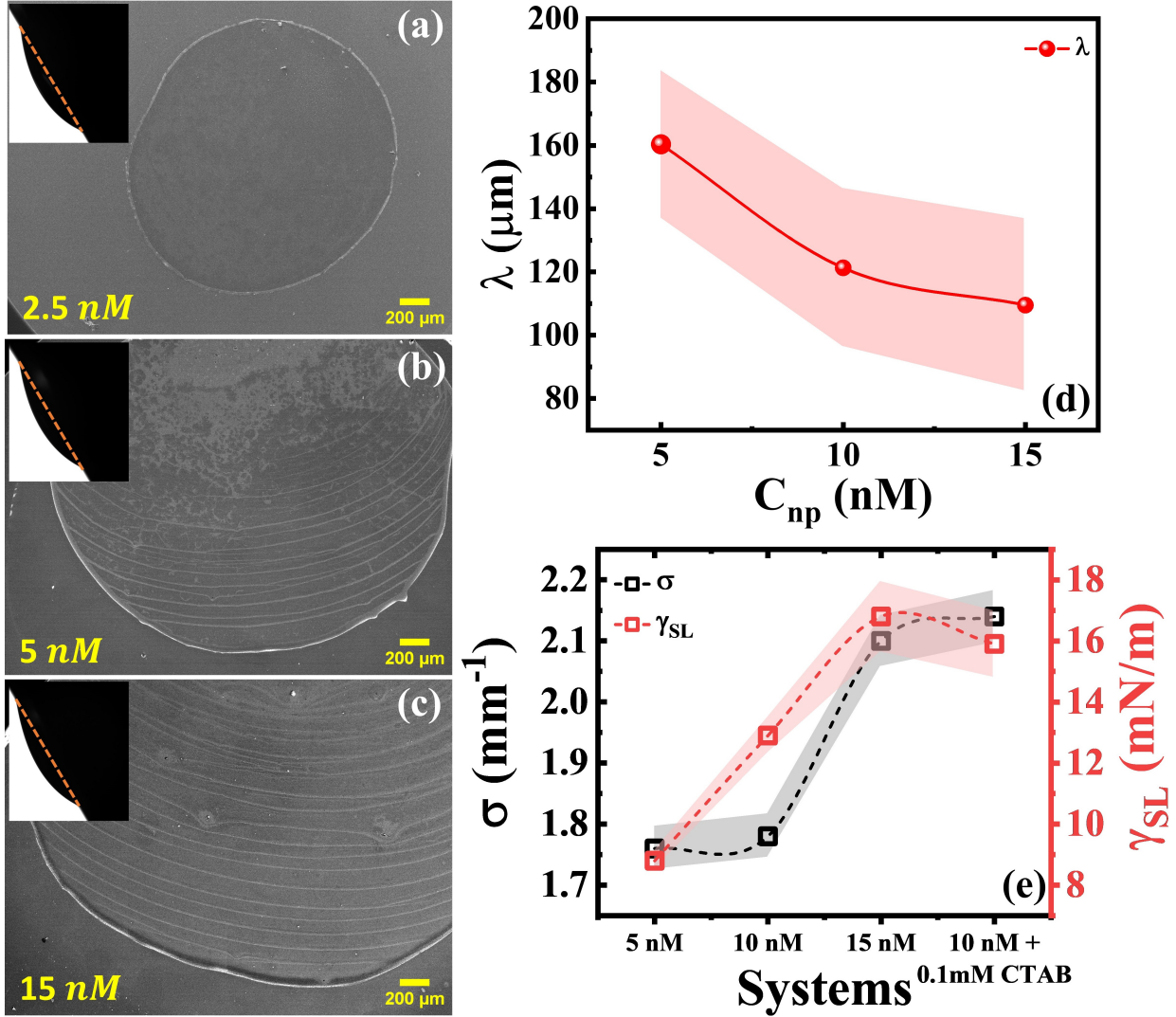


Figure 4: *Ex situ* dried patterns of 2.5, 5, 15 nM AuNP droplets at $\phi = 120^\circ$ are shown in (a-c) [insets showing *in situ* droplet profiles at $t = 0$ s]. Stripes start to form only for $C_{np} \geq 5 \text{ nM}$. Stripe spacing σ decreases with increasing C_{np} (d), indicating enhanced pinning frequency. Consequently, with an increase in C_{np} , stripe density λ increases, and the direct effect of λ and γ_{SL} is established for all the systems (e).

proportional to γ_{SL} , results in TPCL pinning and promotes the formation of denser stripes with increasing C_{np} . With only $F_{g,\parallel}$ variation, nanoparticle density was fixed, resulting in an invariant effect on the TPCL pinning, vis-à-vis λ . But the asymmetry in the droplet shape ($\Delta\theta$) contributes to the normalized σ , showing a sinusoidal trend. These results validate the significance of interfacial tensions in the formation of ordered stripes, while gravity remains uniform. Our results indicate that the dimensions of the stripe patterns, specifically

Table 1: Estimation of γ_{LV} and γ_{SL} with varying particle concentrations (C_{np}) are given below.

C_{np} (nM)	θ_R (°)	γ_{LV} (mN/m)	γ_{SL} (mN/m)
5	23.2	72.7	8.2
10	22.1	67.4	12.6
15	20.3	61.1	17.7
10 + 0.1 mM CTAB	21.1	60.5	18.5

σ and λ , can be controlled by adjusting a single parameter - the surface tension of the sessile drop. Since surface tension can be modulated by altering either the particle density or surfactant concentration within the droplet, we conducted an additional experiment where the liquid–vapor surface tension (γ_{LV}) was reduced by introducing 0.1 mM CTAB. This concentration was carefully chosen to yield an estimate of γ_{SL} comparable to that of the nanoparticle system with $C_{np} = 15$ nM (without added surfactant), enabling direct comparison. As shown in Figure 4(e), the γ_{SL} values in the two cases are nearly identical within the error margin. Notably, the corresponding σ values also fall within a similar range, providing direct evidence for the role of interfacial tension in governing stripe pattern formation with controlled dimensions. Thus, we demonstrate that by fine-tuning surface tension, equivalent striped morphologies can be reproducibly achieved with sub-millimeter precision.

3 Conclusion

In summary, our work offers the first experimental evidence for the creation of semi-circular stripe patterns with controllable dimensions, through solvent evaporation of colloidal droplets on inclined substrates. We provide a correlation between σ , λ , and the experimental parameters such as particle concentration and interfacial tension, thus allowing us to pattern a surface with a stripe-like morphology of desired dimensions. This method shall be useful for various applications that require length scale dependence responses, such as sensing.

While previous studies have observed stick-slip dynamics of the TPCL on inclined substrates,^{11,37} the formation of well-defined, tunable periodic patterns has not been reported.

We show that gravity-driven instability is the driving force for the stick-slip events leading to the formation of stripe patterns. The stripe density σ , mirrors the sinusoidal dependence of the gravitational drag force component on the inclination angle (ϕ). Thus, maximum stripe density is observed at $\phi = 90^\circ$, also correlating with the largest droplet shape asymmetry through $\Delta\theta$. Although gravity controls the stripe density, we have demonstrated that stripe spacing can be controlled by altering interfacial forces. This is achieved by varying the surface tension through changes in particle concentration or by the surfactant concentration, which impact the solid-liquid interfacial tension γ_{SL} . We find that a critical nanoparticle concentration is required for stripe formation, consistent with the analytical relation developed earlier for the occurrence of stick-slip motion on evaporating sessile drop.² By revealing the intricate balance between gravity and interfacial forces in stripe formation, this work establishes a framework for programmable and scalable nanoscale patterning strategies in materials science.

4 Experimental Methods

Materials

Gold (III) chloride trihydrate - $HAuCl_4 \cdot 3H_2O$ ($\geq 99.9\%$) and Trisodium citrate dihydrate - $C_6H_5Na_3O_7 \cdot 2H_2O$ ($\geq 99.0\%$) are obtained from Sigma Aldrich. Hexadecyltrimethylammonium bromide/CTAB - $C_{19}H_{42}BrN$ ($> 98\%$) and Sodium borohydride - $NaBH_4$ ($> 96\%$) were purchased from Spectrochem Pvt Ltd (India). Nitric acid (HNO_3) and hydrochloric acid (HCl) of EMAPRTA grade (Merck), were used for the preparation of aqua regia to clean glassware. Sulphuric acid - H_2SO_4 (98%), Hydrogen peroxide - H_2O_2 (70%) and Acetone (EMAPRTA) were obtained from Merck. Deionized (DI) water (resistivity $18.2\ M\Omega\text{cm}$) is used for all experiments. Silicon wafers (thickness $275 \pm 25\ \mu\text{m}$) are obtained from CEN, IIT Bombay.

Synthesis of AuNPs

The CTAB-coated spherical gold nanoparticles are synthesized using the improvised protocol developed earlier based on seed-mediated growth process.⁴⁶ Citrate-capped seeds are first synthesized, which subsequently generate CTAB-capped larger nanoparticles through ligand exchange. For the seed, $300\ \mu L$ of freshly prepared ice-cold $NaBH_4$ ($0.1\ M$) is introduced into a $10\ mL$ solution containing $0.25\ mM\ HAuCl_4$ and sodium citrate, and the mixture is incubated for 2 hours at room temperature. In parallel, a growth solution consisting of $80\ mM$ CTAB and $0.25\ mM$ gold is prepared, where the temperature may be raised to $50^\circ C$ to facilitate CTAB dissolution but is subsequently cooled to room temperature prior to use. To $45\ mL$ of this growth solution, $0.25\ mL$ of freshly prepared $100\ mM$ ascorbic acid is added under vigorous stirring, followed by the addition of $5\ mL$ of the seed solution. Stirring is done for 10 minutes until the solution turns dark red, after which it is incubated overnight at room temperature. The final growth solution is centrifuged twice at 14000 rpm for 15 minutes to eliminate excess CTAB and other contaminants. Characterizations of the synthesized particles are provided in SI section 1.

Evaporative assembly setup and analysis of deposition patterns

For droplet deposition, a single-side polished $2''\ Si$ wafer was cut into $1\ cm \times 1\ cm$ pieces and cleaned using acetone, Piranha solution (1:1), and a stream of D.I water and dried under N_2 gas. For *in situ* evaporation profile measurements, micro-droplets of nanoparticle suspensions ($2\ \mu L$) were dropcast on freshly cleaned substrate and images of the droplets were recorded through a camera connected to an optical tensiometer (Attension Theta Flex, Biolin Scientific). The evaporation of an inclined colloidal droplet is recorded using a tensiometer stage that can be rotated from $0^\circ - 360^\circ$. For this experiment, the inclination/tilting angle (ϕ) is kept between $0^\circ - 180^\circ$ due to the oscillating nature of sinusoidal functions. Each set of evaporation experiment is repeated several times (≥ 4) to ensure reproducibility and the standard deviations in the measurements are presented as error bars in corresponding plots.

In situ measurements like contact angle (θ), drop diameter (D), and other derived parameters are analyzed by the OneAttension software (Biolin Scientific) using Young-Laplace equation fitting. After the droplet is fully dried, *ex situ* measurements such as FEG-SEM imaging (JEOL JSM-7600F) are done for surface morphology investigation. ImageJ software is used for analyzing SEM micrographs.⁵⁰

Supporting Information

Supporting information includes nanoparticle characterizations, complete inclined-droplet *ex situ* datasets, CRW analysis, γ_{LV} estimation, contact angle and Bond number variations with C_{np} .

Acknowledgement

The authors thank Prof. A. Sain (Dept. of Physics, IIT Bombay) for helpful discussions. The authors acknowledge CSIF IIT Bombay for FEG-SEM and FEG-TEM(200kV/300kV) facilities. SB acknowledges the financial support from CRNTS and IRCC, IIT Bombay. SK acknowledges financial support from the CSIR, India, and IRCC-IIT Bombay. SS acknowledges support from UGC-DAE CSR (CRS/2022-23/03/876), India and IIT Bombay.

Conflict of interest

The authors declare no conflict of interest.

Data Availability Statement

The data that support the findings of this study are available from the corresponding author upon reasonable request.

Keywords

Inclined droplet, evaporative assembly, gold nanoparticle, periodic stripes, tunable assembly.

References

- (1) Guerrero-Martínez, A.; Pérez-Juste, J.; Carbó-Argibay, E.; Tardajos, G.; Liz-Marzán, L. M. Gemini-surfactant-directed self-assembly of monodisperse gold nanorods into standing superlattices. *Angewandte Chemie* **2009**, *121*, 9648–9652.
- (2) Srivastava, S.; Wahith, Z. A.; Gang, O.; Colosqui, C. E.; Bhatia, S. R. Dual-Scale Nanostructures via evaporative assembly. *Advanced Materials Interfaces* **2020**, *7*, 1901954.
- (3) Feng, J.; Qiu, Y.; Jiang, L.; Wu, Y. Long-Range-Ordered Assembly of Micro-/Nanostructures at Superwetting Interfaces. *Advanced Materials* **2022**, *34*, 2106857.
- (4) Zargartalebi, H.; Hejazi, S. H.; Sanati-Nezhad, A. Self-assembly of highly ordered micro- and nanoparticle deposits. *Nature Communications* **2022**, *13*, 3085.
- (5) Elbert, K. C.; Vo, T.; Oh, D.; Bharti, H.; Glotzer, S. C.; Murray, C. B. Evaporation-driven coassembly of hierarchical, multicomponent networks. *ACS nano* **2022**, *16*, 4508–4516.
- (6) Khawas, S.; Bhattacharjee, S.; Mukherjee, S.; Sain, A.; Srivastava, S. Directing the formation of tunable superlattice crystalline phases from anisotropic nanoparticles. *Colloids and Surfaces A: Physicochemical and Engineering Aspects* **2024**, *690*, 133762.
- (7) Watanabe, S.; Inukai, K.; Mizuta, S.; Miyahara, M. T. Mechanism for stripe pattern formation on hydrophilic surfaces by using convective self-assembly. *Langmuir* **2009**, *25*, 7287–7295.

(8) Li, F.; Josephson, D. P.; Stein, A. Colloidal assembly: the road from particles to colloidal molecules and crystals. *Angewandte Chemie International Edition* **2011**, *50*, 360–388.

(9) Zhang, Q.; Uchaker, E.; Candelaria, S. L.; Cao, G. Nanomaterials for energy conversion and storage. *Chemical Society Reviews* **2013**, *42*, 3127–3171.

(10) de Gans, B.-J.; Schubert, U. S. Inkjet printing of well-defined polymer dots and arrays. *Langmuir* **2004**, *20*, 7789–7793.

(11) Winhard, B. F.; Haugg, S.; Blick, R.; Schneider, G. A.; Furlan, K. P. Direct writing of colloidal suspensions onto inclined surfaces: Optimizing dispense volume for homogeneous structures. *Journal of colloid and interface science* **2021**, *597*, 137–148.

(12) Yang, X.; Li, C. Y.; Sun, Y. From multi-ring to spider web and radial spoke: competition between the receding contact line and particle deposition in a drying colloidal drop. *Soft Matter* **2014**, *10*, 4458–4463.

(13) Seo, C.; Jang, D.; Chae, J.; Shin, S. Altering the coffee-ring effect by adding a surfactant-like viscous polymer solution. *Scientific reports* **2017**, *7*, 500.

(14) Kim, D.-O.; Pack, M.; Rokoni, A.; Kaneelil, P.; Sun, Y. The effect of particle wettability on the stick-slip motion of the contact line. *Soft Matter* **2018**, *14*, 9599–9608.

(15) Xu, J.; Xia, J.; Hong, S. W.; Lin, Z.; Qiu, F.; Yang, Y. Self-assembly of gradient concentric rings via solvent evaporation from a capillary bridge. *Physical review letters* **2006**, *96*, 066104.

(16) Mino, Y.; Watanabe, S.; Miyahara, M. T. In Situ observation of meniscus shape deformation with colloidal stripe pattern formation in convective self-assembly. *Langmuir* **2015**, *31*, 4121–4128.

(17) Zhang, S.; Luan, W.; Zhong, Q.; Yin, S.; Yang, F. Evaporation-induced self-assembly of quantum dots-based concentric rings on polymer-based nanocomposite films. *Soft Matter* **2016**, *12*, 8285–8296.

(18) Brown, R.; Orr Jr, F.; Scriven, L. Static drop on an inclined plate: Analysis by the finite element method. *Journal of Colloid and Interface Science* **1980**, *73*, 76–87.

(19) Rotenberg, Y.; Boruvka, L.; Neumann, A. The shape of nonaxisymmetric drops on inclined planar surfaces. *Journal of colloid and interface science* **1984**, *102*, 424–434.

(20) Roura, P.; Fort, J. Equilibrium of drops on inclined hydrophilic surfaces. *Physical Review E* **2001**, *64*, 011601.

(21) Espín, L.; Kumar, S. Sagging of evaporating droplets of colloidal suspensions on inclined substrates. *Langmuir* **2014**, *30*, 11966–11974.

(22) Xie, C.; Zhang, J.; Bertola, V.; Wang, M. Droplet evaporation on a horizontal substrate under gravity field by mesoscopic modeling. *Journal of colloid and interface science* **2016**, *463*, 317–323.

(23) Mamalis, D.; Koutsos, V.; Sefiane, K. On the motion of a sessile drop on an incline: Effect of non-monotonic thermocapillary stresses. *Applied Physics Letters* **2016**, *109*.

(24) Lv, C.; Shi, S. Wetting states of two-dimensional drops under gravity. *Physical Review E* **2018**, *98*, 042802.

(25) Al-Sharafi, A.; Yilbas, B. S.; Ali, H.; AlAqeeli, N. A water droplet pinning and heat transfer characteristics on an inclined hydrophobic surface. *Scientific reports* **2018**, *8*, 3061.

(26) Ravazzoli, P. D.; Cuellar, I.; González, A. G.; Diez, J. A. Contact-angle-hysteresis effects on a drop sitting on an incline plane. *Physical Review E* **2019**, *99*, 043105.

(27) Timm, M. L.; Dehdashti, E.; Jarrahi Darban, A.; Masoud, H. Evaporation of a sessile droplet on a slope. *Scientific reports* **2019**, *9*, 19803.

(28) Cai, J.; Chen, F.; Chamakos, N. T.; Papathanasiou, A. G.; Tan, B.; Li, Q. Asymmetric droplet evaporation on inclined surfaces. *Progress in Nuclear Energy* **2023**, *163*, 104820.

(29) Quéré, D.; Azzopardi, M.-J.; Delattre, L. Drops at rest on a tilted plane. *Langmuir* **1998**, *14*, 2213–2216.

(30) Dhar, P.; Dwivedi, R. K.; Harikrishnan, A. Surface declination governed asymmetric sessile droplet evaporation. *Physics of Fluids* **2020**, *32*.

(31) Du, X.; Deegan, R. Ring formation on an inclined surface. *Journal of Fluid Mechanics* **2015**, *775*, R3.

(32) D'Ambrosio, H.-M.; Wilson, S. K.; Wray, A. W.; Duffy, B. R. Effect of gravity-induced shape change on the diffusion-limited evaporation of thin sessile and pendant droplets. *Physical Review E* **2025**, *111*, 045107.

(33) Chou, T.-H.; Hong, S.-J.; Sheng, Y.-J.; Tsao, H.-K. Drops sitting on a tilted plate: receding and advancing pinning. *Langmuir* **2012**, *28*, 5158–5166.

(34) De Coninck, J.; Fernández-Toledano, J. C.; Dunlop, F.; Huillet, T.; Sodji, A. Shape of pendent droplets under a tilted surface. *Physica D: Nonlinear Phenomena* **2021**, *415*, 132765.

(35) Pan, Z.; Wang, Y. Evaporation of a small water droplet sessile on inclined surfaces. *International Journal of Heat and Mass Transfer* **2022**, *184*, 122330.

(36) Chen, F.; Cai, J.; Chamakos, N. T.; Papathanasiou, A. G.; Gong, Z.; Li, Q. Simulation of asymmetric evaporation of inclined droplets considering natural convection. *Chemical Engineering Science* **2023**, *278*, 118890.

(37) Varagnolo, S.; Ferraro, D.; Fantinel, P.; Pierno, M.; Mistura, G.; Amati, G.; Biferale, L.; Sbragaglia, M. Stick-slip sliding of water drops on chemically heterogeneous surfaces. *Physical review letters* **2013**, *111*, 066101.

(38) Kim, J. Y.; Hwang, I. G.; Weon, B. M. Evaporation of inclined water droplets. *Scientific reports* **2017**, *7*, 42848.

(39) Gopu, M.; Rathod, S.; Namangalam, U.; Pujala, R. K.; Kumar, S. S.; Mampallil, D. Evaporation of inclined drops: formation of asymmetric ring patterns. *Langmuir* **2020**, *36*, 8137–8143.

(40) Kim, J. Y.; Gonçalves, M.; Jung, N.; Kim, H.; Weon, B. M. Evaporation and deposition of inclined colloidal droplets. *Scientific Reports* **2021**, *11*, 17784.

(41) Parsa, M.; Askounis, A. Inclined colloidal drops: Evaporation kinetics and pattern formation. *Frontiers in Mechanical Engineering* **2023**, *9*, 1086544.

(42) Mondal, R.; Semwal, S.; Kumar, P. L.; Thampi, S. P.; Basavaraj, M. G. Patterns in drying drops dictated by curvature-driven particle transport. *Langmuir* **2018**, *34*, 11473–11483.

(43) Bansal, L.; Seth, P.; Sahoo, S.; Mukherjee, R.; Basu, S. Beyond coffee ring: Anomalous self-assembly in evaporating nanofluid droplet on a sticky biomimetic substrate. *Applied Physics Letters* **2018**, *113*.

(44) Hampton, M. A.; Nguyen, T. A.; Nguyen, A. V.; Xu, Z. P.; Huang, L.; Rudolph, V. Influence of surface orientation on the organization of nanoparticles in drying nanofluid droplets. *Journal of colloid and interface science* **2012**, *377*, 456–462.

(45) Hidalgo, R. B. P.; Molina-Courtois, J. N.; Carreón, Y. J.; Díaz-Hernández, O.; González-Gutiérrez, J. Dried blood drops on vertical surfaces. *Colloids and Surfaces B: Biointerfaces* **2024**, *234*, 113716.

(46) Kumar, C.; Bhattacharjee, S.; Srivastava, S. Shape anisotropy induced jamming of nanoparticles at liquid interface: A tensiometric study. *Nanoscale Advances* **2024**,

(47) Tatyanyenko, D. V.; Apitsin, K. D. Line tension from dual-geometry sessile droplet measurements: Combining contact-angle size-dependence data for axisymmetric and cylindrical droplets to determine the line tension. *Physical Review E* **2025**, *111*, 035503.

(48) Al-Sharafi, A.; Yilbas, B. S.; Ali, H.; Al-Qahtani, H. Adhesion of a water droplet on inclined hydrophilic surface and internal fluidity. *International Journal of Adhesion and Adhesives* **2020**, *96*, 102464.

(49) Dunlop, F.; Fatollahi, A. H.; Hajirahimi, M.; Huillet, T. Identities for droplets with circular footprint on tilted surfaces. *Royal Society Open Science* **2020**, *7*, 201534.

(50) Schneider, C. A.; Rasband, W. S.; Eliceiri, K. W. NIH Image to ImageJ: 25 years of image analysis. *Nature methods* **2012**, *9*, 671–675.

Supporting Information[†] to

“Tunable Nanoparticle Stripe Patterns at Inclined Surfaces”

Suman Bhattacharjee,[‡] Sanjoy Khawas,[¶] and Sunita Srivastava^{*,¶}

[‡]*Centre for Research in Nanotechnology & Science (CRNTS), Indian Institute of Technology Bombay, Mumbai-400 076, India*

[¶]*Soft Matter and Nanomaterials Laboratory, Department of Physics, Indian Institute of Technology Bombay, Mumbai-400 076, India*

E-mail: sunita.srivastava@iitb.ac.in

[†]Preprint

1 Characterizations of AuNPs

The synthesized AuNPs are characterized via FEG-SEM and FEG-TEM imaging, UV-Visible spectroscopy, and DLS. Figure S1(a,b) shows the SEM and TEM micrographs for monodisperse AuNPs of size $\sim 15\text{ nm}$, respectively. Figure S1(c) shows the UV-Vis spectra of AuNP colloidal solution, exhibiting an SPR peak at 522 nm . DLS data of the colloidal particles shows a hydrodynamic size of $\sim 33\text{ nm}$, confirming the existence of a hydrated CTAB bilayer around the cores of AuNPs [Figure S1(d)].

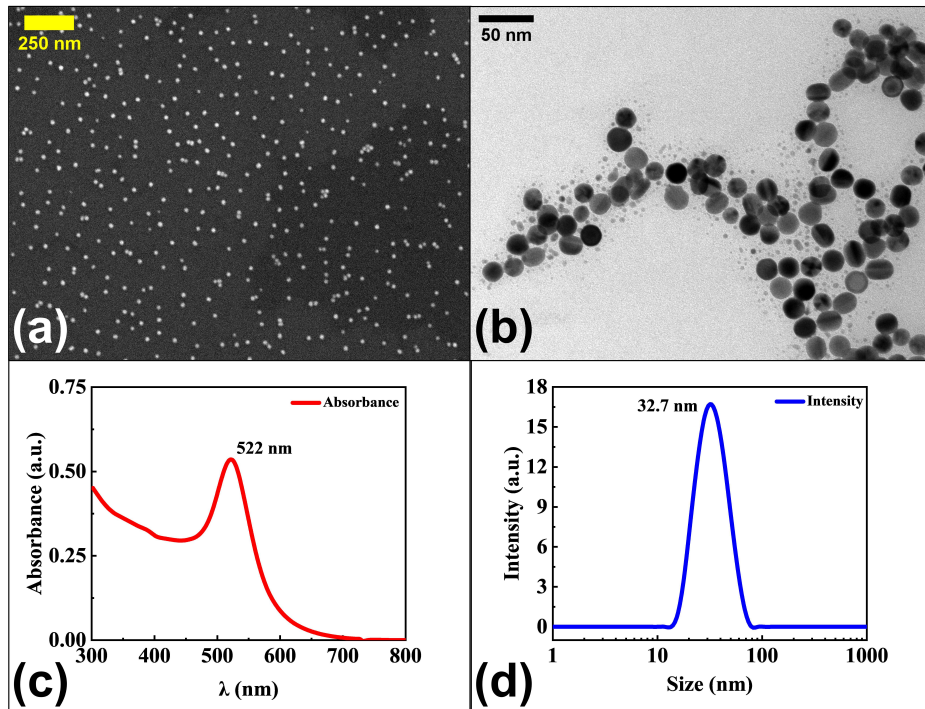


Figure S1: High magnification SEM (a) and TEM image (b) showing spherical CTAB-AuNPs of size $\sim 15\text{ nm}$. UV-Vis absorption spectra (c) show a maximum absorbance peak at 522 nm . DLS shows the hydrodynamic size of spherical AuNPs $\sim 33\text{ nm}$ (d).

2 Dried patterns from inclined droplets: All experimental data

Figure S2(a-e) shows the dependence of gravity on the formation of stripe patterns through the evaporative self-assembly of AuNP droplets. The concentration of AuNP is kept fixed at 15 nM in these experiments. We observe that coffee-ring [Figure S2(a)] and coffee-eye [Figure S2(e)] structure is formed for the sessile ($\phi = 0^\circ$) and pendant drop ($\phi = 180^\circ$), respectively. All the other inclined drops formed striped patterns after drying [Figure S2(b-d)]. The effect of particle concentration, as well as the interfacial tension, is explored to

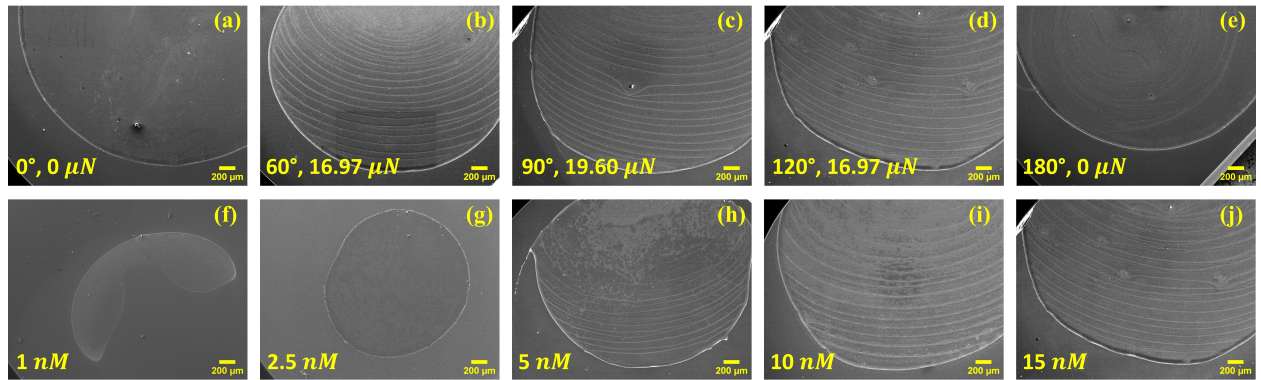


Figure S2: Top panel (a-e) shows the FEG-SEM images of dried deposits of AuNP droplet ($C_{np} = 15 \text{ nM}$) for $\phi = 0^\circ, 60^\circ, 90^\circ, 120^\circ$, and 180° . Bottom panel (f-j) shows the concentration dependence on dried deposits of AuNP droplets at $\phi = 120^\circ$.

understand the stripe pattern formation. A critical concentration $C_{np} = 5 \text{ nM}$ is identified, beyond which the stripes start to form. As can be seen in Figure S2(f-j), coffee-rings are formed without any stripes for particle concentration $C_{np} < 5 \text{ nM}$. For $C_{np} \geq 5 \text{ nM}$, stripes are formed with increasing stripe density [refer to Figure 4(e) in the main text].

3 Gravitational effect on the coffee-ring widths (w)

The effect of gravitational drag is evident in the estimation of coffee-ring widths (w_L, w_R) as presented in Figure S3. The width of the coffee-ring at the left, pinned TPCL (w_L), is

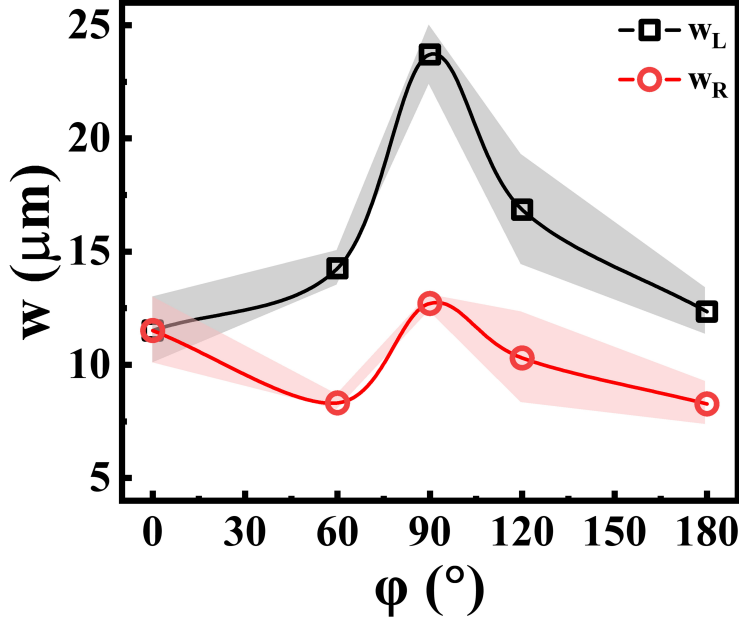


Figure S3: Coffee-ring widths on the left/pinned (w_L) and right/receding side (w_R), are plotted as a function of ϕ .

always estimated to be equal to or higher than the right/receding side width (w_R). The trend in CRW is similar to $\sin \phi$ or $\Delta\theta$, which directly establishes the effect of gravity in the formation of the dried patterns.

4 Estimation of liquid-vapor interfacial tension (γ_{LV}) for different systems

Liquid-vapor interfacial tension (γ_{LV}) is measured using the pendant drop method, which is widely applied to colloidal suspensions at surfaces and interfaces.¹

$$\gamma \left(\frac{1}{R_1} + \frac{1}{R_2} \right) = \Delta p_0 - \Delta \rho g z \quad (\text{S1})$$

For a pendant drop at equilibrium [Eq. S1], the Laplace pressure across the interface is given by $\Delta p \equiv \Delta p_0 - \Delta \rho g z$. Here, Δp denotes the pressure difference at $z = 0$ relative to the hydrostatic pressure ($\rho g z$). $\Delta \rho$ is the density difference between the liquid (ρ_l) and the

surrounding phase (ρ_a), while g is the gravitational acceleration. The surface (or interfacial) tension is experimentally determined by fitting the drop profile geometrically [Figure S4] using Eq. S1.

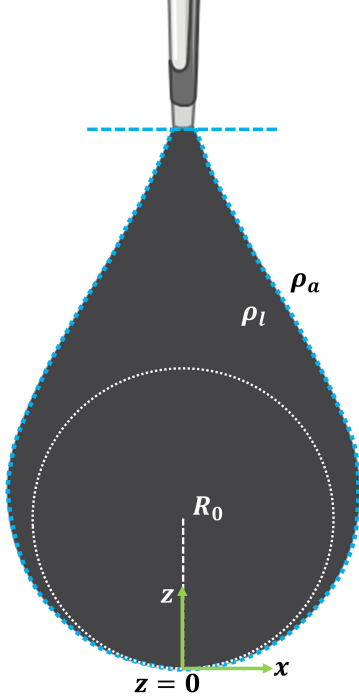


Figure S4: Schematic of a pendant drop with Young-Laplace fitting for the estimation of γ_{LV} .

5 Variation in contact angles (θ) and Bond number (B_o) with AuNP concentrations (C_{np})

As observed in our experiments, stripe patterns are only formed beyond a critical particle concentration of 5 nM. Figure S5(a) shows the variations in θ_L , θ_R , and $\Delta\theta$ with increasing C_{np} . As the droplets are pinned from the beginning, R_0 is approximately the same for all cases at constant gravitational drag ($\phi = 120^\circ$, $F_{g,\parallel} = 16.97 \mu N$). θ_R values are always $< 25^\circ$, from where the stick-slip motion is happening. A constant trend in the $\Delta\theta$ values suggests equivalent gravitational effect on all the drops. The decline in the θ_R denotes the

influence of particle concentration (C_{np}), which can be correlated to the decrease in γ_{LV} .

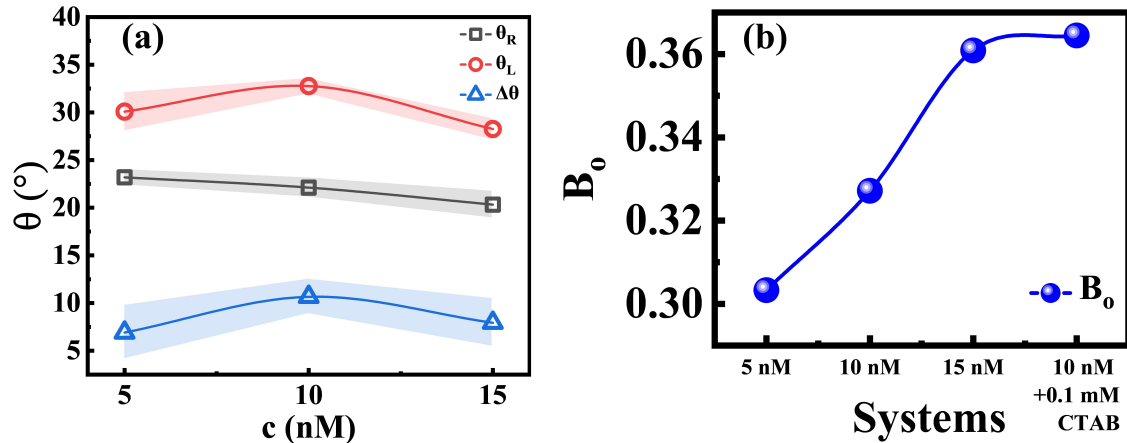


Figure S5: Dependence of θ_L , θ_R and $\Delta\theta$ with AuNP concentration are shown in (a). Calculated B_o for different systems are plotted in (b).

Bond number (B_o) is the ratio of gravitational force to the surface tension force, and is defined as $B_o = R^2 \rho g / \gamma_{LV}$. Figure S5(b) shows the variation in B_o from for different systems, signifying almost equivalent effect of gravity ($B_o \approx 0.30 - 0.36$) while surface tension dominates.

References

- (1) Pan, Z.; Trusler, J. M.; Jin, Z.; Zhang, K. Interfacial property determination from dynamic pendant-drop characterizations. *Nature Protocols* **2024**, 1–24.